Optimisation and control of electric ship microgrids with short-term energy storage systems

Hardan, Faysal; Tricoli, Pietro

[Link to publication on Research at Birmingham portal](#)

Optimisation and control of electric ship microgrids with short-term energy storage systems

Faysal Hardan, Pietro Tricoli, *Senior Member, IEEE*

Abstract—The inertia of DC power system is very low in general compared to the traditional AC system's inertia, necessitating the introduction of new concepts for shipboard DC power systems. This paper proposes an innovative control structure for electric-ship DC system which integrates ultra-capacitor and SMES energy storage systems to stabilise its microgrid with minimal voltage disturbance caused by the ship dynamic loads, whilst allowing dynamic close-loop re-balancing of the storage systems. New design and optimisation methodologies, based on new dynamic system model, are presented and discussed. Power system performance has been assessed and validated through real-time hardware-in-the-loop simulation and practical implementation of the control concept using DSP hardware.

Index Terms—Battery service life, control system, electric vessel, energy storage, power electronic converter, propulsion, shipboard DC power system, stability, superconducting magnetic energy storage, thrusters, ultracapacitors.

I. INTRODUCTION

IN response to climate change, many governmental agencies worldwide have adopted policies and plans to decarbonise the transport sector. Maritime transport mostly relies on fossil fuels that substantially contribute to carbon emissions. Therefore, there is an increasing demand for zero-emission vessels powered by batteries or hybrid sources including other types of energy storage. However, batteries have limited charging/discharging cycles and are expensive to replace at their end-of-life service. Therefore, research to focus on extending their service life is highly desirable to reduce the total cost of ownership of electric vessels. Recent research and studies have reported on the utilisation of ultra-capacitor/ supercapacitor energy storage in battery powered systems for efficient operation and to extend the operational lifespan of the batteries [1-5]. In general, ultra-capacitors have higher number of charging cycles when compared with batteries, and they can be charged or discharged rapidly to handle the dynamic power of ship propulsion motors [6-8]. Current advancement in ultra-capacitor (UC) technology has led to increasing energy densities, with current figures above 4.3Wh/L, and power densities about 15kW/L [9]. In comparison, superconducting magnet energy storage (SMES) produced by Si microfabrication technology can achieve

Faysal Hardan is with Department of Electronic, Electrical, and Systems Engineering, University of Birmingham, UK (e-mail: f.hardan@bham.ac.uk).

Pietro Tricoli is with Department of Electronic, Electrical, and Systems Engineering, University of Birmingham, UK (e-mail: p.tricoli@bham.ac.uk).

Color versions of one or more of the figures in this article are available online at http://ieeexplore.ieee.org

energy density in the range of 1Wh/L [10]. Research and applications of hybrid energy storage systems (ESSs) to combine UC and SMES with batteries onboard electric vehicles (EV) have been reported widely in literature, e.g., in [11-16]. In [11], the proposed battery/UC system uses a small DC/DC converter controlled as an energy pump for setting the UC voltage at a level higher than the battery voltage for dynamic driving. As such, the battery only provides power to the load when the UC voltage drops below the battery voltage, causing almost constant load profile for the battery. However, the DC-bus voltage in this system can vary widely to gain benefit from the stored UC energy, which is not preferred for voltage-regulated DC power systems. An example of SMES in battery powered bus is reported in [12], where the author proposed a power control algorithm to improve battery lifetime. Research reported in [13] attempted to validate the effectiveness of battery-UC hybrid ESS for EV applications by analysing the influence of battery prices with different operating temperatures on optimising the hybrid ESS, including UC size and energy management system. References [14] and [15] cover considerable reviews of ESSs for application in EVs, including batteries, UC, SMES and key management issues. However, for integrating ESSs into ship power systems, different AC/DC power architectures have been studied and reported in the literature, e.g., in [17] and [18]. They can be designed with hierarchical and zonal control and protection, which have been the subject of current and recent research activities of marine and shipboard applications [19], [20].

The most important issue for the DC shipboard power system is the stabilisation of its DC voltage, associated with the inherent low inertia of the DC systems. In this context, a variety of control, coordination, and power management methods were proposed and studied, including those for hybrid ESSs [21-26]. In the presence of pulsating electric loads on ships, articles [27-32] report on the control and management of hybrid ESSs and shipboard power systems, including modelling at different levels. In [27], the authors proposed a virtual admittance droop control based on the traditional virtual resistor and capacitor droop method, where the hybrid ESS mitigates the transient power fluctuations of the loads. Notably, article [31] reports on the application of hybrid SMES/battery ESS in all-electric ship to improve the stability of its DC power system, using dynamic droop control for prioritising the charging or discharging process.

This paper proposes an innovative control structure for electric-ship DC power system which integrates UC energy storage (UCES) and SMES systems to stabilise the microgrid
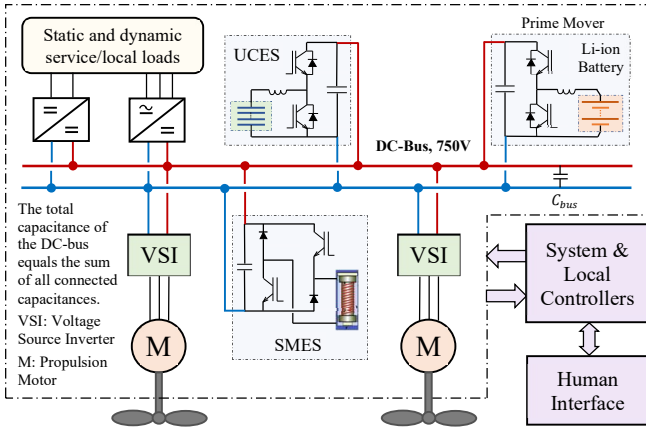
Fig.1. The architecture and its components for the ship DC power system.

voltage of the system with minimal voltage disturbance caused by the ship transient/dynamic loads. This structure includes a new mechanism with cross-coupling control, which allows the storage systems to re-balance their charging states through the microgrid DC-bus in an indirect closed-loop manner. To realise this structure, a new dynamic model of the DC power system has been derived with analysis. A new optimisation method for the coupling control has also been proposed, with design and stability analysis based on the derived system model as presented and discussed in later sections of the paper. The control concept has been validated through DSP hardware implementation, interfaced to a hardware-in-the-loop (HiL) platform that was programmed to represent the components of the DC power system for real-time simulation. The system included a DC microgrid, battery, UCES, SMES, their power electronic (PE) converters, and the vessel's dynamic propulsion load.

II. The Architecture of the Ship Power System

The considered architecture of the ship power system, which accommodates the vessel battery, ESSs, propulsion units and loads, is illustrated in Fig.1. It has been adopted with common-bus type, which is usually considered for ships equipped with electric propulsion motors/generators [33]. With this type of architecture, it is efficient to absorb the regenerative power by the ESSs when the motor is stopped, or its rotational direction is reversed. The block diagram in Fig.1 only represents a simplified microgrid DC-bus for the ship's DC switchboard without redundancy. The Li-ion battery in the diagram represents the prime mover of the ship and it is interfaced to the main DC-bus via its controllable DC-DC PE converter. The vessel service/local loads are supplied from the DC-bus through their DC-DC and DC-AC converters adjusted to the voltage levels required for service equipment. The electric propulsion/thruster units were considered to utilise induction machines as motors/generators, which are powered and controlled by electric drives. These drives are based on voltage-source-inverters (VSIs) and the field-oriented control for high-performance torque control and operational characteristics [34]. As illustrated, the UCES and SMES are

connected directly to the DC-bus through their own PE converters for easy exchange of transient and regenerative power with the thruster drives. As the vessel power system is inherently isolated from the onshore grid, the simplest transformerless converter topologies were adopted onboard to minimise the number of PE devices and to obtain the highest possible efficiency for the power system. Therefore, the half-bridge buck-boost PE topology was selected for the battery and UCES converters, whereas a parallel buck-boost topology (as illustrated in Fig.1) was employed for the SMES converter. The converter topologies can be based on either Si IGBT or SiC MOSFET devices, integrated or packaged within half-bridge and full-bridge modules. System and local controllers, including those for the UCES, SMES, and DC-voltage, deliver control signals to the relevant power converters and motor inverters based on measurement of the controlled variables. The values of the UC capacitance and SM inductance were chosen to be similar and equal to 10F and 10H for symmetry and simplicity of design, optimization, analysis, and comparison. Based on these values, both UCES and SMES can store energy up to 1.8MJ each for the case-study presented in this paper.

III. The Proposed Control Structure and Dynamic System Modelling

For modelling purposes, the block diagrams in Fig.2 have been configured to represent the proposed control structure of the ship's DC power system. Each box of the diagrams represents either a sub-system or control function of the overall control structure, and it is indicated with its specific input and output variables. These boxes are linked according to their input/output signal flow to ease the process for dynamic modelling of the system with the required control functions. As can be realised from the upper diagram, the
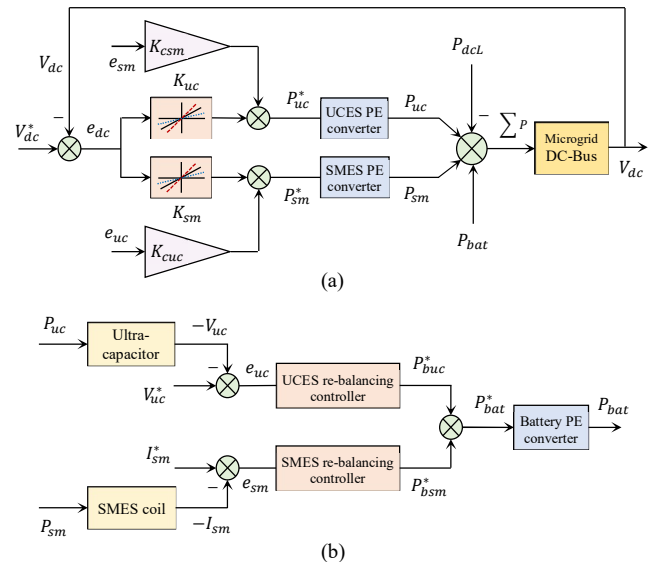

(a)

(b)

Fig.2. A block-diagram representing the overall proposed control structure: (a): the main closed-loop control section for stabilising the microgrid DC-bus voltage via the UCES and SMES systems, (b): the re-balancing control loop for the UC voltage and SMES coil current. The variables with asterisk '*' represent references or demand quantities.

control structure considers stabilising the DC-bus voltage directly via the UCES and SMES PE converters through bi-directional adjustments of their output power to the microgrid DC-bus. The power references for the power controllers of these systems can be derived using DC voltage-droop controllers represented by gains K_{uc}, K_{sm}. Normally, these gains should generate bidirectional power demands with maximum level equivalent to the ESS nominal power when the DC-bus voltage deviation reaches its upper and lower limits of ±10% [18], [32], which is equivalent to ±0.1 per-unit. Therefore, if the power demand and DC-bus voltage are represented using the per-unit system, the gains can be set to 10 to produce maximum/minimum power demands of ±1 per-unit when the DC voltage deviation reaches its limits. The power demand-signals are fed to the power or current controllers of the PE converters, which control the power flow of the energy storage elements. To re-balance the UCES voltage and SMES current, the battery must deliver the long-term power to the DC power system, which is equivalent to the average DC-load plus power losses. As the UCES and battery are regarded as voltage sources, they can both have identical PE converters and power controller structures. The reference-voltage signals produced by the power controllers are pulse-width-modulated (PWM) to control the PE switches of their half-bridge PE converters. However, as the SMES is regarded as a current source, the SMES PE converter must be capable of circulating the SMES current for dynamic operation. The coupling factors K_{cuc}, K_{csm} were introduced to guarantee that both the UCES and SMES systems are working in parallel, and their stored energies are shared equally without being one of them depleted before the other. More details about validating the functionality of these factors are covered and demonstrated in later parts of this paper.

The block diagrams in Fig.3 illustrates the power-controller structures of the UCES and SMES PE converters. It should be noted that the UCES and SMES power controllers are non-linear in general because the division by v_{uc} and i_{sm}, which are variables affected by their controlled current i_{uc} and
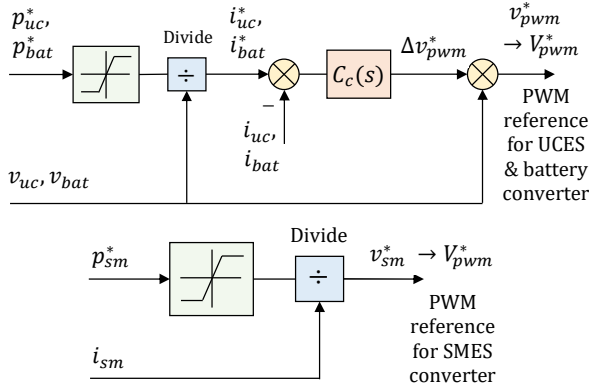
p_{uc}^*, v_{uc}, i_{uc}: are the UCES power demand, voltage and current,
$p_{bat}^*, v_{bat}, i_{bat}$: are the battery power demand, voltage and current,
$i_{sm}, p_{sm}^*, v_{sm}^*$: are the SMES current & its power and voltage demands,
$C_c(s)$: is a current controller function.

Fig.3. Block diagrams representing the UCES, battery, and SMES power/ current controllers that deliver the PWM reference voltage signals.

voltage v_{sm}, respectively. However, these variables change slowly due the large UC capacitance and SMES inductance. As such, the power controllers exhibit linear behaviour around the set-points of the UC voltage and SMES current.

A. The DC-Bus Power-Voltage Model

The DC-bus electrical model can be described by the following differential equation,

$$C_{dc} \frac{dv_{dc}}{dt} = i_{cdc} - G_c v_{dc} \qquad (1)$$

v_{dc} is the DC-bus voltage and i_{cdc} is the current that flows into or from the total DC-bus capacitance C_{dc}. This current is the algebraic sum of all currents of the UCES, SMES, battery, and DC load exchanged with the microgrid DC-bus. The term $G_c v_{dc}$ represents the leakage current through this capacitance's conductance G_c. Considering that v_{dc} is kept close to its nominal value during the normal operation, then multiplying both sides of the above equation by the nominal value of the microgrid DC-bus voltage v_{dcn} results in the following power-voltage expression.

$$C_{dc} v_{dcn} \frac{dv_{dc}}{dt} \cong p_{uc} + p_{sm} + p_{bat} - p_{dcL} - G_c v_{dcn} v_{dc} \quad (2)$$

p_{uc}, p_{sm}, p_{bat}, p_{dcL} are the instantaneous values of the UCES, SMES, battery, and DC load power, respectively. When both sides of this equation are divided by the nominal power of the microgrid DC-bus p_{dcn}, the equation can be converted to a per-unit power-voltage model as follows.

$$\frac{dV_{dc}}{dt} + \frac{G_c}{C_{dc}} V_{dc} \cong \frac{1}{2H_{dc}} (P_{uc} + P_{sm} + P_{bat} - P_{dcL}) \qquad (3)$$

The voltage and power variables are given here in capital letters to denote per-unit quantities. The DC load power P_{dcL} represents all the vessel's loads consumed and exchanged through the connecting DC-bus. The quantity H_{dc} is the inertia constant of the DC power system and is defined as

$$H_{dc} = \frac{\frac{1}{2} C_{dc} v_{dcn}^2}{p_{dcn}}.$$

B. The Ultra-capacitor Power-Voltage Model

As short-term ESSs, ultra-capacitors are mainly designed to provide high specific power. Therefore, their equivalent series-resistance is usually very small and can be neglected. However, to account for self-discharging losses of the UC, a conductance connected in parallel to it can be added. Based on this consideration, the dynamic model of the UC can be reduced to the following first-order differential equation.

$$\frac{dv_{uc}}{dt} = \frac{-1}{C_{uc}} i_{cuc} - \frac{G_{uc}}{C_{uc}} v_{uc} \qquad (4)$$

v_{uc}, i_{cuc}, C_{uc}, G_{uc} are the voltage, output current, capacitance, and parallel conductance of the UC, respectively. Considering that the UC is working around its nominal voltage v_{ucn} (which will be the case), the following power-voltage expression can be obtained by multiplying both sides of equation (4) by v_{ucn}.

$$v_{ucn} \frac{dv_{uc}}{dt} = \frac{-1}{C_{uc}} p_{cu} - \frac{G_{uc}}{C_{uc}} v_{ucn} v_{uc} \qquad (5)$$

p_{uc} is the UC output power. Dividing both sides of the equation by the nominal power of the UC p_{ucn} and re-

arranging its terms, the per-unit power-voltage model of the UC can be derived as

$$\frac{dV_{uc}}{dt} + \frac{G_{uc}}{C_{uc}} V_{uc} \cong \frac{-1}{2H_{uc}} P_{uc} \qquad (6)$$

V_{uc}, P_{uc} are the UC per-unit voltage and power, respectively, and H_{uc} represents the inertia constant of the UCES system,

$$H_{uc} = \frac{\frac{1}{2} C_{uc} v_{ucn}^2}{p_{ucn}}.$$

It is worthwhile to mention that the UC power P_{uc} is regarded approximately equivalent to the UCES system power as the efficiency of the UCES PE converter is usually very close to 100%. This will also be considered for the PE converters of the SMES and battery systems when deriving their models in the next sub-sections.

C. The SMES Power-Current Model

The superconducting coil of an SMES system is cooled down below its critical temperature by the system's cryogenic unit to transfer the coil's wire to the superconducting state, which is associated by almost zero wire resistance. From a mathematical modelling point of view, this coil can be represented by an inductance L_{sm} with a highly small resistance r_{sm}, connected to it in series manner. Accordingly, the voltage across the coil can be modelled mathematically as follows.

$$L_{sm} \frac{di_{sm}}{dt} + r_{sm} i_{sm} = -v_{sm} \qquad (7)$$

i_{sm} is the coil current and v_{sm} is the voltage across it applied by the SMES PE converter in the negative direction to extract power from the SMES system. As the coil will be utilised around its nominal current i_{smn}, then multiplying both sides of the above equation by this current results in the following power-current form,

$$L_{sm} i_{smn} \frac{di_{sm}}{dt} + r_{sm} i_{smn} i_{sm} = -p_{sm} \qquad (8)$$

p_{sm} is the output power of the SMES system as the coil is charged/discharged with current around i_{smn}. Dividing both sides of the above expression by the SMES nominal power p_{smn} and re-arranging its terms, the following per-unit power-current model of the SM coil can be derived,

$$\frac{dI_{sm}}{dt} + \frac{r_{sm}}{L_{sm}} I_{sm} \cong \frac{-1}{2H_{sm}} P_{sm} \qquad (9)$$

I_{sm}, P_{sm} are the coil per-unit current and power, respectively, and H_{sm} represents the inertia constant of the SMES system,

$$H_{sm} = \frac{\frac{1}{2} L_{sm} i_{smn}^2}{p_{smn}}.$$

It should be noted that the resistance of the SMES coil was substituted for zero in the subsequent sections for system analysis and design, but it was included here for modelling purposes only.

D. Derivation of the Battery Power Model

The re-balancing controllers of the UCES and SMES were selected to be as simple as possible with an integrating memory term to drive the energy storage error to zero after a certain time determined by the capacity of the UC and SMES coil.

Accordingly, the proportional-integral (PI) function was found suitable for both the UCES and SMES re-balancing controllers. The design procedure for selecting the most appropriate gains of the PI function is discussed in a subsequent section. According to the block diagrams of Fig.2 and their input/output variables, and by considering the PI law for the UCES and SMES re-balancing controllers, the following expressions can be worked out.

$$\frac{dP_{buc}^*}{dt} = -K_{puc} \frac{dV_{uc}}{dt} + K_{iuc}(V_{uc}^* - V_{uc}) \qquad (10)$$

$$\frac{dP_{bsm}^*}{dt} = -K_{psm} \frac{dI_{sm}}{dt} + K_{ism}(I_{sm}^* - I_{sm}) \qquad (11)$$

where, P_{buc}^*, P_{bsm}^* are battery power demands generated by the UCES and SMES re-balancing controllers, K_{puc} and K_{iuc} are the proportional and integral gains of the UCES re-balancing controller, and K_{psm}, K_{ism} are the gains for the SMES re-balancing controller. The variables with the asterisk '*' represent references or demand quantities. Substituting the voltage and current derivatives from equations (6) and (9) into equations (10) and (11), it can be found that,

$$\frac{dP_{buc}^*}{dt} = \frac{K_{puc}}{2H_{uc}} P_{uc} + \left(\frac{K_{puc} G_{uc}}{C_{uc}} - K_{iuc}\right) V_{uc} + K_{iuc} V_{uc}^* \qquad (12)$$

$$\frac{dP_{bsm}^*}{dt} = \frac{K_{psm}}{2H_{sm}} P_{sm} + \left(\frac{K_{psm} r_{sm}}{L_{sm}} - K_{ism}\right) I_{sm} + K_{ism} I_{sm}^* \qquad (13)$$

As illustrated in the lower block diagram of Fig.2. the battery power demand and its derivative can be expressed as

$$P_{bat}^* = P_{buc}^* + P_{bsm}^* \rightarrow \frac{dP_{bat}^*}{dt} = \frac{dP_{buc}^*}{dt} + \frac{dP_{bsm}^*}{dt} \qquad (14)$$

For system analysis and design purposes, it is acceptable to consider that the power bandwidth of the PE battery converter is high enough so that its response delay can be neglected. As such, the battery power P_{bat} can be approximately equivalent to its power demand P_{bat}^*, and so forth for its power derivative. Therefore, the following expression can be considered for modelling the battery power based on equation (14).

$$\frac{dP_{bat}}{dt} \cong \frac{dP_{bat}^*}{dt} = \frac{dP_{buc}^*}{dt} + \frac{dP_{bsm}^*}{dt} \qquad (15)$$

Adopting similar response characteristics of the re-balancing controllers leads to selecting similar set of gains for both controllers, i.e.,

$$K_{puc} = K_{psm} = K_p \; , \; K_{iuc} = K_{ism} = K_i \; .$$

Accordingly, one re-balancing controller may be used for both the UC voltage and SMES current error signals. However, the re-balancing controllers can be generally designed with different set of gains for different response characteristics. Substituting the similar set of controller gains K_p and K_i into equations (12) & (13), and then substituting the resulting expressions into equation (15), gives the following dynamical sub-model for the produced battery power.

$$\frac{dP_{bat}}{dt} = \left(\frac{K_p G_{uc}}{C_{uc}} - K_i\right) V_{uc} + \left(\frac{K_p r_{sm}}{L_{sm}} - K_i\right) I_{sm} +$$

$$\frac{K_p}{2H_{uc}} P_{uc} + \frac{K_p}{2H_{sm}} P_{sm} + K_i V_{uc}^* + K_i I_{sm}^*. \qquad (16)$$

E. The Full State-Space Model of the Power System

The above mathematical expressions can form the system dynamic-model derived according to the signal flow illustrated on the block diagrams of Fig.2, which shows all the sub-systems involved in the closed-loop control process. Combining all sub-system models, a single state-space model can be formulated which is useful for system analysis and design of the DC voltage and re-balancing controllers. Considering that the UCES and SMES PE converters have an ideal step-response, the following equations can be realised according to Fig.2 diagrams.

$$P_{uc} \cong P_{uc}^* = K_{uc}\,(V_{dc}^* - V_{dc}) + K_{csm}\,(I_{sm}^* - I_{sm}) \quad (17)$$

$$P_{sm} \cong P_{sm}^* = K_{sm}\,(V_{dc}^* - V_{dc}) + K_{cuc}\,(V_{uc}^* - V_{uc}) \quad (18)$$

K_{uc} and K_{sm} are the DC-bus voltage-droop gains of the UCES and SMES control channels, and K_{csm} and K_{cuc} are the coupling factors into these channels, respectively. Substituting the above equations into equations (3), (6) and (9) results in the following expressions for the state-space model of the whole system,

$$\frac{dV_{dc}}{dt} = -\left\{\frac{G_c}{C_{dc}} + \frac{(K_{uc}+K_{sm})}{2H_{dc}}\right\}V_{dc} - \frac{K_{cuc}}{2H_{dc}}V_{uc} - \frac{K_{csm}}{2H_{dc}}I_{sm} +$$

$$\frac{P_{bat}}{2H_{dc}} + \frac{(K_{uc}+K_{sm})}{2H_{dc}}V_{dc}^* + \frac{K_{cuc}}{2H_{dc}}V_{uc}^* + \frac{K_{csm}}{2H_{dc}}I_{sm}^* - \frac{P_{dcL}}{2H_{dc}} \quad (19)$$

$$\frac{dV_{uc}}{dt} = -\frac{G_{uc}}{C_{uc}}V_{uc} + \frac{K_{uc}}{2H_{uc}}V_{dc} + \frac{K_{csm}}{2H_{uc}}I_{sm} -$$

$$\frac{K_{uc}}{2H_{uc}}V_{dc}^* - \frac{K_{csm}}{2H_{uc}}I_{sm}^* \quad (20)$$

$$\frac{dI_{sm}}{dt} = -\frac{r_{sm}}{L_{sm}}I_{sm} + \frac{K_{sm}}{2H_{sm}}V_{dc} + \frac{K_{cuc}}{2H_{sm}}V_{uc} -$$

$$\frac{K_{sm}}{2H_{sm}}V_{dc}^* - \frac{K_{cuc}}{2H_{sm}}V_{uc}^* \quad (21)$$

$$\frac{dP_{bat}}{dt} = -\left(\frac{K_p K_{uc}}{2H_{uc}} + \frac{K_p K_{sm}}{2H_{sm}}\right)V_{dc} + \left(\frac{K_p\,G_{uc}}{C_{uc}} - \frac{K_p K_{cuc}}{2H_{sm}} - K_i\right)V_{uc} +$$

$$\left(\frac{K_p\,r_{sm}}{L_{sm}} - \frac{K_p K_{csm}}{2H_{uc}} - K_i\right)I_{sm} + \left(\frac{K_p K_{uc}}{2H_{uc}} + \frac{K_p K_{sm}}{2H_{sm}}\right)V_{dc}^* +$$

$$\left(K_i + \frac{K_p K_{cuc}}{2H_{sm}}\right)V_{uc}^* + \left(\frac{K_p K_{csm}}{2H_{uc}} + K_i\right)I_{sm}^*. \quad (22)$$

Using the common state-space notation [35], the model can be expressed as

$$\frac{dx(t)}{dt} = A\,x(t) + B\,u(t) \quad (23)$$

$$Y(t) = C\,x(t); \quad (24)$$

$$x(t) = [V_{dc}\quad V_{uc}\quad I_{sm}\quad P_{bat}]^T$$

$$u(t) = [V_{dc}^*\quad V_{uc}^*\quad I_{sm}^*\quad P_{dcL}]^T$$

$A =$

$$\begin{bmatrix} \frac{-G_c}{C_{dc}} - \frac{K_{uc}+K_{sm}}{2H_{dc}} & \frac{-K_{cuc}}{2H_{dc}} & \frac{-K_{csm}}{2H_{dc}} & \frac{1}{2H_{dc}} \\ \frac{K_{uc}}{2H_{uc}} & \frac{-G_{uc}}{C_{uc}} & \frac{K_{csm}}{2H_{uc}} & 0 \\ \frac{K_{sm}}{2H_{sm}} & \frac{K_{cuc}}{2H_{sm}} & \frac{-r_{sm}}{L_{sm}} & 0 \\ \frac{-K_p K_{uc}}{2H_{uc}} - \frac{K_p K_{sm}}{2H_{sm}} & \frac{K_p\,G_{uc}}{C_{uc}} - \frac{K_p K_{cuc}}{2H_{sm}} - K_i & \frac{K_p\,r_{sm}}{L_{sm}} - \frac{K_p K_{csm}}{2H_{uc}} - K_i & 0 \end{bmatrix}$$

$$B = \begin{bmatrix} \frac{K_{uc}+K_{sm}}{2H_{dc}} & \frac{K_{cuc}}{2H_{dc}} & \frac{K_{csm}}{2H_{dc}} & \frac{-1}{2H_{dc}} \\ \frac{-K_{uc}}{2H_{uc}} & 0 & \frac{-K_{csm}}{2H_{uc}} & 0 \\ \frac{-K_{sm}}{2H_{sm}} & \frac{-K_{cuc}}{2H_{sm}} & 0 & 0 \\ \frac{K_p K_{uc}}{2H_{uc}} + \frac{K_p K_{sm}}{2H_{sm}} & K_i + \frac{K_p K_{cuc}}{2H_{sm}} & \frac{K_p K_{csm}}{2H_{uc}} + K_i & 0 \end{bmatrix}$$

$Y(t)$ is the output vector of the model, C is a 4×4 identity matrix, and T denotes a matrix transpose. It can be realised that the input vector elements V_{dc}^*, V_{uc}^* and V_{sm}^* will be set to a fixed value of one per-unit as the system is intended to operate around the nominal values. However, the input element P_{dcL}, which is the vessel load power, can vary rapidly according to the thruster loads. Based on this closed-loop model of the system, the generic transfer functions of the full system in s-domain can be obtained.

$$Y(s) = G(s)\,U(s) \quad (25)$$

$$U(s) = [\Delta V_{dc}^*(s)\quad \Delta V_{uc}^*(s)\quad \Delta I_{sm}^*(s)\quad \Delta P_{dcL}(s)]^T$$

$$Y(s) = [\Delta V_{dc}(s)\quad \Delta V_{uc}(s)\quad \Delta I_{sm}(s)\quad \Delta P_{bat}(s)]^T$$

$$G(s) = \begin{bmatrix} g_{11}(s) & g_{12}(s) & g_{13}(s) & g_{14}(s) \\ g_{21}(s) & g_{22}(s) & g_{23}(s) & g_{24}(s) \\ g_{31}(s) & g_{32}(s) & g_{33}(s) & g_{34}(s) \\ g_{41}(s) & g_{42}(s) & g_{43}(s) & g_{44}(s) \end{bmatrix}$$

where, $G(s)$ represents the matrix of the I/O transfer functions and Δ denotes a change in the relevant variable. Amongst the input variables, only the DC-load will be changing due to vessel loads and/or thruster power, and the transfer functions which connect this input to the system outputs are g_{14}, g_{24}, g_{34}, and g_{44}. Noting that the most significant output dynamics for analyse are the dynamics of the DC-bus voltage and battery power, it was suitable to only consider the relevant transfer functions, g_{14} from input P_{dcL} to output V_{dc}, and g_{44} from input P_{dcL} to output P_{bat}.

$$g_{14}(s) = N_{14}(s)/D_n(s) \quad (26)$$

$$g_{44}(s) = N_{44}(s)/D_n(s) \quad (27)$$

$$N_{14}(s) = b_{10}\,s^3 + b_{11}\,s^2 + b_{12}\,s + b_{13} \quad (28)$$

$$D_n(s) = a_0\,s^4 + a_1\,s^3 + a_2\,s^2 + a_3\,s + a_4 \quad (29)$$

$$N_{44}(s) = b_{40}\,s^2 + b_{41}\,s + b_{42}\,; \quad (30)$$

$$b_{10} = \frac{-1}{2H_{dc}},\; b_{11} = \frac{-G_{uc}}{2H_{dc}\,C_{uc}} - \frac{r_{sm}}{2H_{dc}\,L_{sm}},$$

$$b_{12} = \frac{K_c^2}{8H_{dc}\,H_{sm}\,H_{uc}} - \frac{G_{uc}\,r_{sm}}{2H_{dc}\,C_{uc}\,L_{sm}},\; b_{13} = 0\,.$$

$$a_0 = 1\,,\; a_1 = \frac{K_d}{H_{dc}} + \frac{G_c}{C_{dc}} + \frac{G_{uc}}{C_{uc}} + \frac{r_{sm}}{L_{sm}},$$

$$a_2 = \frac{-K_c^2}{4H_{sm}H_{uc}} + \frac{K_d(K_c+K_p)}{4H_{dc}H_{uc}} + \frac{K_d(K_c+K_p)}{4H_{dc}H_{sm}} + \frac{G_{uc}K_d}{H_{dc}C_{uc}} + \frac{G_c G_{uc}}{C_{dc}C_{uc}} +$$
$$\frac{K_d r_{sm}}{H_{dc}L_{sm}} + \frac{G_c r_{sm}}{C_{dc}L_{sm}} + \frac{G_{uc}r_{sm}}{C_{uc}L_{sm}},$$

$$a_3 = \frac{-G_c K_c^2}{4C_{dc}H_{sm}H_{uc}} + \frac{K_d K_i}{4H_{dc}H_{uc}} + \frac{K_d K_i}{4H_{dc}H_{sm}} + \frac{K_d K_c K_p}{4H_{dc}H_{sm}H_{uc}} +$$
$$\frac{G_{uc}K_d(K_c+K_p)}{4H_{dc}H_{sm}C_{uc}} + \frac{r_{sm}K_d(K_c+K_p)}{4H_{dc}H_{uc}L_{sm}} + \frac{G_{uc}K_d r_{sm}}{H_{dc}C_{uc}L_{sm}} + \frac{G_c G_{uc}r_{sm}}{C_{dc}C_{uc}L_{sm}},$$

$$a_4 = \frac{K_c K_d K_i}{4H_{dc}H_{sm}H_{uc}} + \frac{G_{uc}K_d K_i}{4H_{dc}H_{sm}C_{uc}} + \frac{K_d K_i r_{sm}}{4H_{dc}H_{uc}L_{sm}}.$$

$$b_{40} = \frac{K_d K_p}{4H_{dc}H_{uc}} + \frac{K_d K_p}{4H_{dc}H_{sm}},$$

$$b_{41} = \frac{K_d K_i}{4H_{dc}H_{uc}} + \frac{K_d K_i}{4H_{dc}H_{sm}} + \frac{K_d K_c K_p}{4H_{dc}H_{sm}H_{uc}} + \frac{G_{uc}K_d K_p}{4H_{dc}H_{sm}C_{uc}} +$$
$$\frac{r_{sm}K_d K_p}{4H_{dc}H_{uc}L_{sm}},$$

$$b_{42} = \frac{K_d K_c K_i}{4H_{dc}H_{sm}H_{uc}} + \frac{G_{uc}K_d K_i}{4H_{dc}H_{sm}C_{uc}} + \frac{r_{sm}K_d K_i}{4H_{dc}H_{uc}L_{sm}}.$$

IV. OPTIMISED SELECTION OF COUPLING FACTORS

The coupling factors K_{cuc} and K_{csm} were integrated within the control structure to dynamically equalise the per-unit errors of the stored energies within the UCES and SMES, preventing them from depleting/rising before each other. To find the optimum values of these factors, an objective function F for minimising the difference between the errors of the UC voltage and SMES current has been derived. This function is based on squaring the per-unit difference between the UC voltage error and the SMES current error:

$$F(V_{uc}, I_{sm}, t) = \frac{1}{2}\left\{ \begin{bmatrix} (V_{uc}^* - V_{uc}(t)) \end{bmatrix} - \\ [(I_{sm}^* - I_{sm}(t))] \end{bmatrix} \right\}^2 \qquad (31)$$

From dynamic-control point of view, minimising this function at all times of operation requires that its derivative with respect to time should be equal to zero.

$$min\ F \rightarrow \frac{dF}{dt} = 0\ , or,$$

$$[(V_{uc}^* - V_{uc}) - (I_{sm}^* - I_{sm})] \cdot \left(\frac{dI_{sm}}{dt} - \frac{dV_{uc}}{dt} \right) = 0. \qquad (32)$$

Considering only the part of the derivatives of V_{uc} and I_{sm}, which can be substituted from equations (6) and (9), and replacing P_{uc} and P_{sm} for their expressions in (17) and (18), which involve the coupling factors K_{cuc} and K_{csm}, the following expressions can be derived,

$$\frac{dV_{uc}}{dt} = \frac{-G_{uc}}{C_{uc}}V_{uc} - \frac{1}{2H_{uc}}[K_{uc}e_{dc} + K_{csm}(I_{sm}^* - I_{sm})] \qquad (33)$$

$$\frac{dI_{sm}}{dt} = \frac{-r_{sm}}{L_{sm}}I_{sm} - \frac{1}{2H_{sm}}[K_{sm}e_{dc} + K_{cuc}(V_{uc}^* - V_{uc})] \qquad (34)$$

For the study presented in this paper, the DC voltage-droop gains were considered equal, and the same was also applied to the coupling factors, i.e., $K_{uc} = K_{sm} = K_d$, and $K_{cuc} = K_{csm} = K_c$. Substituting equations (33) and (34) into (32), and simplifying the final expression, the optimal coupling factor K_c (as a function of V_{uc} and I_{sm}) can be calculated as follows,
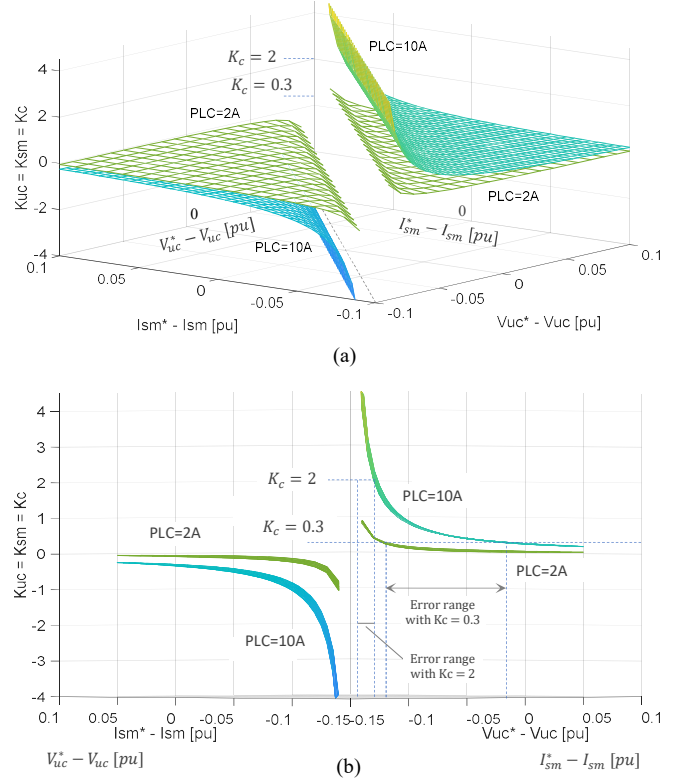

(a)

(b)

Fig.4. Variation of the common coupling factor K_c as function of the errors of V_{uc} and I_{sm} at different values of parallel leakage current of the UCES; V_{uc}^* and I_{sm}^* were set to 1 per-unit, and $K_d = 10$.

$$K_c(V_{uc}, I_{sm}) = \frac{e_{dc}K_d\left(\frac{1}{2H_{uc}} - \frac{1}{2H_{sm}}\right) + \frac{G_{uc}}{C_{uc}}V_{uc} - \frac{r_{sm}}{L_{sm}}I_{sm}}{\frac{(V_{uc}^* - V_{uc})}{2H_{sm}} - \frac{(I_{sm}^* - I_{sm})}{2H_{uc}}}. \qquad (35)$$

It is worth noting that the per-unit values V_{uc}^* and I_{sm}^* are equal to one when set and fixed to their relevant nominal values. Around the nominal operating points, the above expression is discontinuous and is a function of the UC voltage V_{uc} and SMES current I_{sm}. As can be realised, the effect of the DC-voltage error e_{dc} on K_c is negligible when the inertia constants of the UC and SMES systems are close in values. In fact, according to equation (35), K_c can be affected considerably by the difference between the UC leakage current $G_{uc}V_{uc}$ and the SMES dropping voltage $r_{sm}I_{sm}$. And when passing an additional parallel leakage current (PLC) out of the UC, this can clearly help to demonstrate how the calculated value of the coupling factor can be affected. Considering two additional PLCs at 2A and 10A, and using the system parameters provided in Table II of Section VII for equation (35), the 3-D graphs in Fig.4(a) demonstrate how K_c is changing whilst V_{uc} and I_{sm} errors are varying in the range $\{-0.1 \cdots 0.1\}$ per-unit. When the errors of the UCES voltage and SMES current are close to each other, the optimal value of K_c is relatively high until it becomes uncertain. In other words, K_c should be high enough to minimise the difference between the errors of V_{uc} and I_{sm}. The graph in Fig.4(b) is a rotated-up version of the previous 3-D graph around V_{uc} and I_{sm} error axes, which can help to illustrate the concentration of the optimum values of K_c. It can be realised that the selected value for K_c depends on the PLC magnitude and the designer's preferred

range of acceptable difference between the V_{uc} and I_{sm} errors. Within the PLC range from 2A to 10A, the author recommended a range of optimal values for K_c between 0.3 and 2, as indicated by the dotted lines in Fig.4(b). Accordingly, this would allow acceptable differences between the UCES voltage and SMES current errors within limits around ±0.05 per-unit. It should be noted that selecting negative values for the coupling factor K_c will render the system unstable. Therefore, the negative range of K_c in Fig.4 has been excluded. For system analysis, design and testing in the following sections, K_c was given the value of one ($K_c = 1$) which was found reasonable under the operating conditions presented in the paper.

V. SYSTEM ANALYSIS AND CONTROLLER DESIGN

A. System Dynamics without Re-balancing Controllers

To analyse the system behaviour without invoking the UCES and SMES re-balancing controllers, the controllers' gains K_p and K_i have been set to zero to exclude the action of the re-balancing controllers. This means that there is no battery power produced by the battery PE converter and the re-balancing control loop is completely open. As a result, the system model has been characterised by only three poles. Using the system parameters as given in Table II of Section VII, these poles are all located in the left half of the complex plane, which indicate that the system is stable under this condition. The first pole p_1 is equal to -178 and is associated with the DC-bus dynamics and its voltage-droop gains, whilst poles p_2 and p_3 are equal to -0.0494 and -0.0000043, respectively. These last two poles are mainly affected by the values of the UCES capacitance and SMES inductance, and the coupling factor K_c.

B. System Dynamics with Re-balancing Controllers

To check the system dynamics for close-loop control including the re-balancing mechanism, the characteristic equation (29) of the close-loop system model has been solved at different values of gains K_p & K_i as given in Table I. Accordingly, different groups of system poles have been obtained for analysis and design selection of the most suitable set of gains. As shown in the table, the first and second poles p_{c1}, p_{c2} of the system seem to be unaffected by the changes in gains K_p & K_i, and are equal to the first and second poles associated with the system without the re-balancing controllers. In fact, p_{c1}, p_{c2} are only relevant to the DC voltage control-loop represented by the diagram in Fig.2 (a), and only affected by the loop gains and parameters. These poles are negative real values that do not cause any stability or oscillation issues to the system. However, the third and fourth poles p_{c3}, p_{c4} of the system are mostly conjugate poles close to the origin of the complex plane, causing a lightly damped oscillation with low frequency. This frequency can be shifted to a lower level by decreasing the value of the integrating gain K_i.
As can be realised from Table I, these complex poles can be shifted further to the left half of the complex plane by increasing the proportional gain K_p for more damping. Notably, at value of K_p around 0.3, with integrator gain K_i equals 0.001, the system poles p_{c3}, p_{c4} become completely negative real values, which render the system output non-oscillatory. This situation will be considered and discussed further in association with the step-response analysis covered in the next sub-section.

TABLE I
SYSTEM POLES BASED ON ITS DYNAMIC MODEL AT DIFFERENT CONTROLLER GAINS

Controller Gains	System model poles: $p_{c1}, p_{c2}, p_{c3}, p_{c4}$		
	$K_{cuc} = K_{csm} = K_c = 1$		
	Common poles for all gains: $p_{c1} = -178$, $p_{c2} = -0.0494$		
	p_{c3} , p_{c4}		
K_p	$K_i = 0.001$	$K_i = 0.005$	$K_i = 0.01$
0.1	$-0.00247 \pm j0.00658$	$-0.00247 \pm j0.0155$	$-0.00247 \pm j0.0221$
0.2	$-0.00494 \pm j0.005$	$-0.00494 \pm j0.0149$	$-0.00494 \pm j0.0217$
0.3	$-0.00977, -0.00506$	$-0.00741 \pm j0.0138$	$-0.00741 \pm j0.0209$
0.4	$-0.0168, -0.00293$	$-0.00988 \pm j0.0122$	$-0.00988 \pm j0.0199$
0.5	$-0.0225, -0.00219$	$-0.01235 \pm j0.0097$	$-0.01235 \pm j0.0185$

C. Response Analysis

The references of the DC-bus voltage V_{dc}^*, UC voltage V_{uc}^* and SMES current I_{sm}^*, were all set to their nominal values in this study. Considering that the sub-models are linear around these values, the references will always take the value of 1 per-unit when utilising the per-unit system. The most relevant dynamic responses to analyse for the DC power system are the responses of the DC-bus voltage and battery power to step change in the DC-load power P_{dcL}. For this purpose, the system transfer functions g_{14} and g_{44} in equations (26) and (27) have been utilised to generate the step responses in time-domain. The graphs in Fig.5 and Fig.6 illustrate the step responses of the DC voltage and battery power in response to 0.1pu step change in P_{dcL}; all at different values of gain K_p and fixed gain K_i. It can be realised from Fig.5 that in all illustrated cases the changes in the DC voltage did not exceed 2.3%, and the oscillation is more dampened as the value of gain K_p is increased. This analysis agrees with the system characteristics associated with poles p_{c3}, p_{c4} in the previous sub-section. In Fig.6, the battery power responses clearly illustrate that the final changes in the battery power P_{bat} are all equivalent to the step change in the DC-load power P_{dcL}, which conform to the aim of the proposed control structure. Traces 3 of both Fig.5 and Fig.6 demonstrate that when using set of gains $K_p = 0.3$ & $K_i = 0.001$, the responses are non-oscillatory, which can be a design option for these gains. However, it should be noted that as K_p increases, the battery power rises or changes with less delay, which may not be a preferred case as most of the energy capacity range of the UCES and SMES systems may not be properly utilised.

VI. SYSTEM HiL SIMULATION AND CONTROL IMPLEMENTATION

To validate and assess the proposed control concept, including the performance of the UCES and SMES systems and their power controllers, a detailed real-time hardware-in-the-loop (HiL) simulation has been performed for the ship DC power system. This covered the DC-microgrid, battery, controllable thruster load, UC, SMES coil, and their PE converters, which are indicated in the block diagram of Fig.1. The HiL real-time simulation was based on a Typhoon platform, whilst the designed control system has been implemented within the
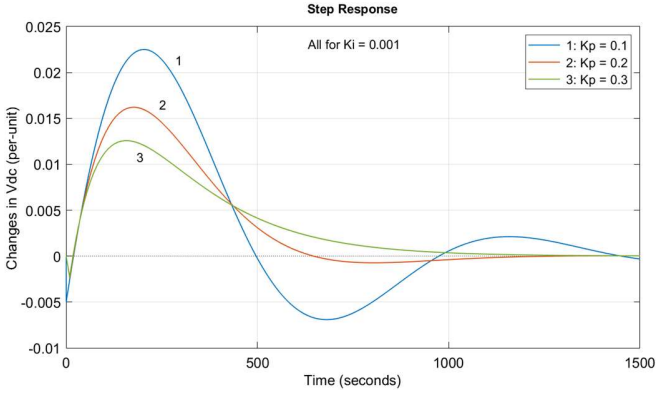
TTE-Reg-2023-05-1075

Fig.5. Step response from input P_{dcL} at 0.1pu to output V_{dc} for different values of controller gain K_p with fixed value of K_i at 0.001.
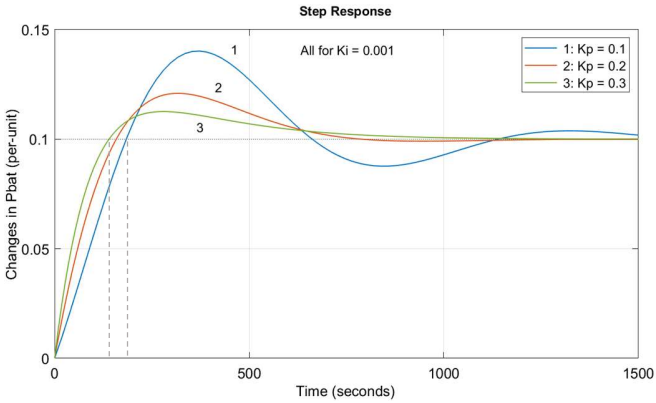

Fig.6. Step response from input P_{dcL} at 0.1pu to output P_{bat} for different values of controller gain K_p with fixed value of K_i at 0.001.

Delfino TI DSP - F28379D board interfaced to this platform as illustrated in Fig.7. To run system testing and operation, both power and control parts on the Typhoon HiL platform and within the DSP board must be run simultaneously. Measurement of the system outputs/variables can be monitored and recorded directly via a multi-channel digital oscilloscope or through the control software of the DSP board.

A. The Real-Time HiL Simulation

The parts of the DC power system were implemented and connected within the Typhoon HiL schematic editor using its library components and PE blocks, with updating interval lower than 500ns. The UC and Li-ion battery have been represented by the supercapacitor and battery blocks, respectively, which are already available within the editor library. To represent the SMES unit, an inductance with zero internal resistance was employed to resemble a superconducting coil. Both battery and UC blocks were connected to half-bridge IGBT converters through a 3mH inductance for buck-boost operation, whilst the coil inductance block was driven using full-bridge PE converter with unidirectional-current operation. The controllable thruster load was controlled through an independent task implemented within the DSP board. This task executed the equivalent dynamic model of the thruster's mechanical drivetrain in real-time with 10kHz updating rate. As such, this has reflected the actual dynamics of the vessel thruster according to the system physical parameters and operational scenarios. Some details on
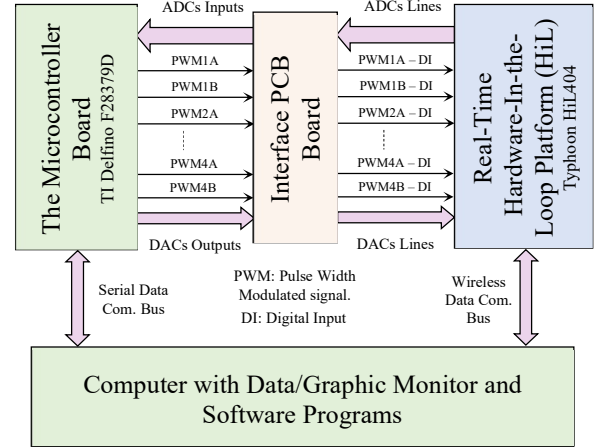

Fig.7. A block-diagram representing system implementation using TI Microcontroller board, interfacing card and HiL platform - all programmed and monitored through a lab computer.

this drivetrain model and its torque signal generation are provided in Section VII.

B. Implementation of the System Controllers

The practical implementation of the UCES, SMES, and battery controllers, including the relevant PWM generators for their PE converters, has been carried out utilising the DSP board with I/O signals as illustrated in Fig.7. Feedback measurement of all voltage and current variables, generated by the real-time HiL simulator was performed through the board's 12bit ADC channels, scanned at 10kHz sampling rate. The output variables generated by the control algorithms are converted by the board to PWM signals to drive the PE devices of the converters through the external digital inputs of the HiL platform. This arrangement reflects the exact practical environment for testing the operation and performance of the system and controllers under various operational scenarios.

VII. TEST RESULTS AND ANALYSIS

Based on the implementation and settings described above, various testing power scenarios were applied to the system, represented by different transient/dynamic thruster power. The thrusting power component considered in testing the proposed control structure and system, was generated using the dynamic model representing the thruster drivetrain with a total moment of inertia J and mechanical damping factor B. The considered parameters and specification of the equivalent thruster model are given in Table II. To derive this model, the torque response-time of the thruster PE motor drive was ignored as it is very low in comparison with the time-constant of the mechanical drivetrain.

TABLE II
SPECIFICATIONS AND MAIN DESIGN PARAMETERS OF THE STUDIED SHIP DC POWER SYSTEM AND ITS COMPONENTS

Microgrid DC-bus	Nominal voltage: 750V, Maximum power: 1MW, Total DC-bus capacitance: $C_{dc} = 0.04F$, Conductance of total capacitance: $G_c = 10^{-3}\Omega^{-1}$
Li-ion battery pack	Nominal energy capacity: 500kW/h, Nominal voltage: 400V.

Ultra-capacitor ESS	Capacitance: $C_{uc} = 10F$, Conductance of ultra-capacitor: $G_{uc} = 12 \times 10^{-6}\Omega^{-1}$, Nominal power: 100kW, Voltage range: 200V to 600V, Nominal voltage: 450V, Max stored energy: 1.8MJ.
SMES	Coil inductance: $L_{sm} = 10H$, Resistance of the SM coil: $r_{sm} = 0\Omega$, Nominal power: 100kW, Current range: 200A to 600A, Nominal current: 450A, Max stored energy: 1.8MJ.
Control gains	$K_{uc} = K_{sm} = K_d = 10$, $K_{cuc} = K_{csm} = K_c = 1$, $K_p = 0.3$, $K_i = 0.001$

Thruster system: Maximum shaft speed: 800 rpm, Total moment of inertia J: 10 kg.m², Total mechanical damping B: 0.9 N.m.s/rad

The equivalent load torque of the drivetrain shafts was considered to have a quadratic relationship with the shaft speed. The input or reference torque to this model was formed as a repeated stepwise sequence, generated randomly with normal distribution at 2s sampling time for 30s duration. To present the results clearly, the generated torque values were approximately rounded to the nearest value points of 0, ±0.25, ±0.5, ±0.75 and ±1 per-unit for power in the range {-200kW to 200kW}. As a result, the output of the drivetrain model has generated the corresponding thrust power, which has been utilised to obtain the testing results presented in this section. The implemented control structure and power components of the system were all initialised with the parameters and system specifications

provided in Table II. Firstly, the whole system has been run and tested without utilising the coupling factors, i.e., when $K_c = 0$. The obtained testing graphs are presented in Fig.8, which included traces of recorded data for the voltage, current and power variables of all relevant parts of the power systems as indicated in the figure. The presented traces within the time window between 560s and 585s, clearly illustrate the operation and performance of the system whilst the thrust power is changing rapidly each 2s. Trace 1 in graphs (a) demonstrates that the microgrid DC-bus voltage stayed within the allowed limit ±10% (i.e., between 675V and 825) all times. The battery current is almost fixed around an average value whilst the UCES current and SMES voltage are highly varying to provide the required trust power. The ripples superimposed within the current and voltage traces were mainly caused by the measurement noise and bias. Traces 2 and 3 of graph (a) are the measured UC voltage and SMES coil current, respectively, which demonstrate how these variables are changing slowly whilst delivering the required power to the DC-bus. It is important to note that due to the UC parallel leakage current, the UC voltage was shifted down and it is not compensated by the control system as the functionality of the coupling factors was inhibited. Graph (b) of Fig. 8, illustrates the corresponding power traces of the UCES, SMES and battery power in response to the varying thrust power. It can be realised that both UCES and SMES power are changing equivalently according to the intended specification, whilst the battery power is almost constant around its average
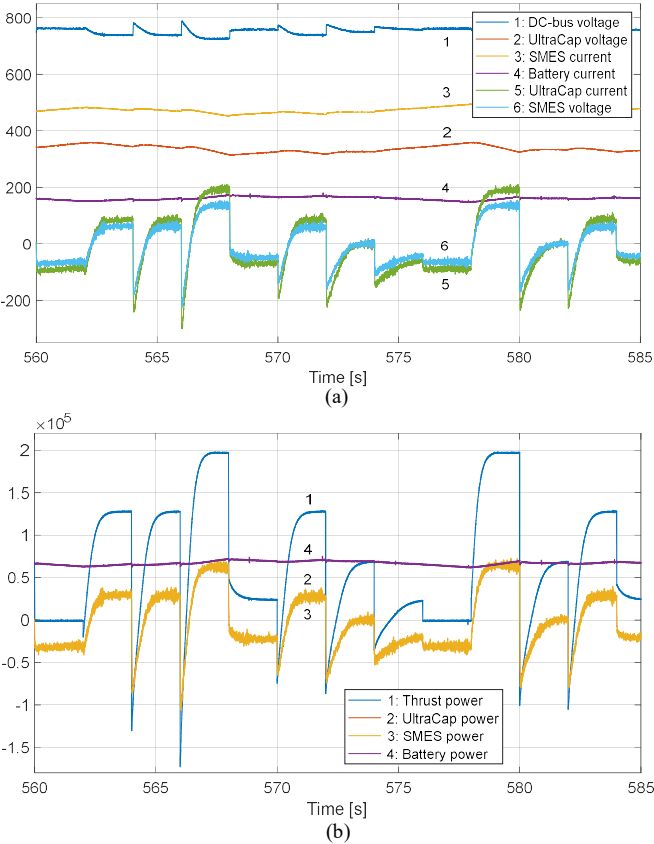

Fig.8. Test results without coupling factors, with 10A UC leakage current: (a) traces of the DC-bus, UCES, and SMES voltages, and their currents, (b) traces of the thrust, UCES, SMES, and battery power.
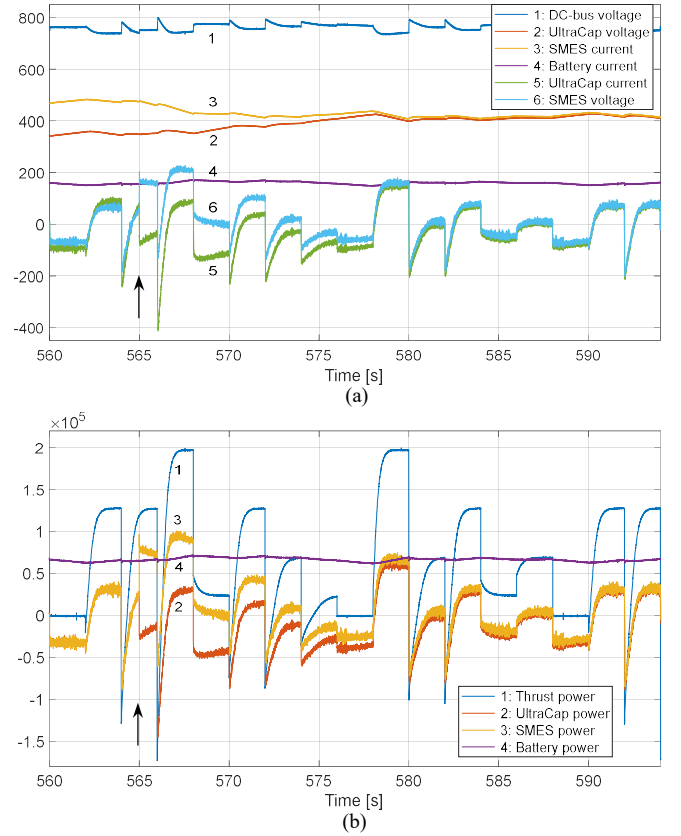

Fig.9. Test results on the transition state when the functionality of the coupling factors was enabled with $K_c = 1$ at time 565s: (a) traces of the DC-bus, UCES, and SMES voltages, and their currents, (b) traces of the thrust, UCES, SMES, and battery power.
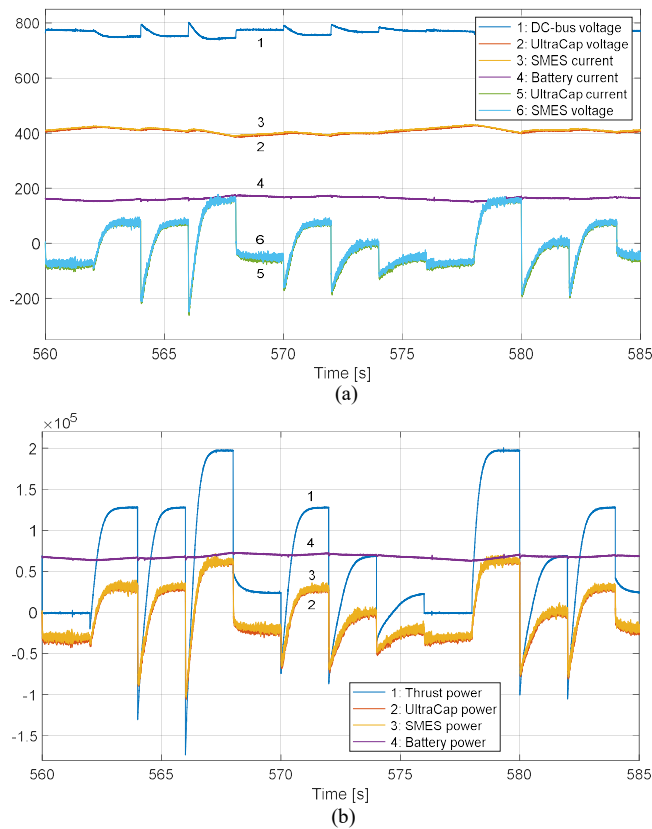
TTE-Reg-2023-05-1075

Fig.10. Test results demonstrate the continuous operation of the system with coupling factors equal to one, and how the energy storage level of the UCES and SMES systems (indicated by their voltage and current – traces 2, 3) stay closed to each other.

level. At any point of time, the sum of the UCES, SMES and battery power is approximately equal to the thrust power, as the service load are set to zero during all dynamic tests presented in the paper. At some instants, the UCES and SMES power became negative in response to the regenerative power when the drivetrain propellers of the ship suddenly change their spinning direction. These dynamic results sound in a good agreement with the design and required performance criteria.

Secondly, to demonstrate the functionality and effectiveness of the coupling factors, the whole implemented system was run up to 565s when the coupling factors were enabled at this time with $K_c = 1$, as shown in Fig.9. After this time, graph (a) clearly illustrates the transition state of the ultra-capacitor voltage and SMES current as they start to move closer to each other, as the functionality of the coupling factors was active. It can be realised that the DC-bus voltage and battery current are not affected, whilst the SMES voltage was increasing in magnitude during the transition state to discharge the SMES more than the UC. This condition was also reflected on the SMES power as illustrated by trace 3 in graph (b) until the compensation process was almost completed at time around 590s. The response time for compensation with $K_c = 1$, was around 25s whilst the UC leakage current was set to 10A. These results clearly demonstrate the functionality and performance of the coupling factors within the proposed control structure. The graphs of Fig.10 demonstrate the continuous operation of the designed system with coupling

factors equal to one, and how the UC voltage and SMES current stayed close to each other in graph (a). Accordingly, the stored energies of the UCES and SMES systems will vary equally in similar manner, as both systems were designed with 10F capacitance and 10H inductance, and with the same nominal voltage and current. It is clearly illustrated in graph (b) that the power consumed by the battery remained almost steady, with acceptable fluctuation around its average level, whilst the thrust power was changing rapidly. It is worthwhile to mention that maintaining the battery current at an average level would lead to reduced ohmic or heat losses within the battery, which is proportional to the squared value of its current. As such, this would help to maintain the battery performance and to extend its service life [36].

VIII. CONCLUSION

This paper presented an integrated control structure for DC power system stabilisation in battery-powered electric ships utilising short-term energy storage. It considered ultra-capacitor and SMES systems to primarily stabilise the DC system voltage, whilst forcing the battery current to follow closely an average level of the vessel dynamic load. As battery power/heat losses are caused by its internal resistance, shaving its peak currents would reduce these losses, leading to higher efficiency and lower internal temperature. From control point of view, both UCES and SMES systems delivered almost the same power-control performance, although they utilised different PE converter topologies. Also, it has been proven that the operations of the local and second-tier controllers within the DSP board have been efficient for driving the HiL-simulated power system within the HiL platform. And the obtained results have demonstrated the effectiveness of the proposed control concept to stabilise the ship power system under harsh operational scenarios, accompanied with transient thrust/load power.

REFERENCES

[1] R. Carter, A. Cruden and P. J. Hall, "Optimizing for Efficiency or Battery Life in a Battery/Supercapacitor Electric Vehicle," in IEEE Transactions on Vehicular Technology, vol. 61, no. 4, pp. 1526-1533, May 2012, doi: 10.1109/TVT.2012.2188551.

[2] D. Lemian and F. Bode, "Battery-Supercapacitor Energy Storage Systems for Electrical Vehicles: A Review," *Energies*, vol. 15, no. 15, p. 5683, Aug. 2022, doi: 10.3390/en15155683.

[3] I. Stadler, M. Sterner, "Urban Energy Storage and Sector Coupling," in *Urban Energy Transition*, 2nd ed., P. Droege Ed., Elsevier, 2018, ch. 2, sec. 3, pp. 225-244.

[4] H. Xu, M. Shen, "The control of lithium-ion batteries and supercapacitors in hybrid energy storage systems for electric vehicles: A review," International Journal of Energy Research, Vol. 45, no. 15, pp. 20524-20544, Aug. 2021, doi: 10.1002/er.7150.

[5] A. S. Sener, "Improving the Life-Cycle and SOC of the Battery of a Modular Electric Vehicle Using Ultra-Capacitor," 2019 8th International Conference on Renewable Energy Research and Applications

(ICRERA), Brasov, Romania, 2019, pp. 611-614, doi: 10.1109/ICRERA47325.2019.8996616.

[6] J. Hou, J. Sun and H. F. Hofmann, "Mitigating Power Fluctuations in Electric Ship Propulsion With Hybrid Energy Storage System: Design and Analysis," in IEEE Journal of Oceanic Engineering, vol. 43, no. 1, pp. 93-107, Jan. 2018, doi: 10.1109/JOE.2017.2674878.

[7] S. Faddel, A. A. Saad, M. E. Hariri and O. A. Mohammed, "Coordination of Hybrid Energy Storage for Ship Power Systems With Pulsed Loads," in IEEE Transactions on Industry Applications, vol. 56, no. 2, pp. 1136-1145, March-April 2020, doi: 10.1109/TIA.2019.2958293.

[8] Z. Dong, X. Cong, Z. Xiao, X. Zheng and N. Tai, "A Study of Hybrid Energy Storage System to Suppress Power Fluctuations of Pulse Load in Shipboard Power System," 2020 International Conference on Smart Grids and Energy Systems (SGES), Perth, Australia, 2020, pp. 437-441, doi: 10.1109/SGES51519.2020.00083.

[9] S.I. Wong, J. Sunarso, B.T. Wong, H. Lin, A. Yu, B. Jia, "Towards enhanced energy density of graphene-based supercapacitors: Current status, approaches, and future directions," Journal of Power Sources, vol. 396, pp. 182-206, 2018, doi: 10.1016/j.jpowsour.2018.06.004.

[10] T. Motohiro, M. Sasaki, J. Noh, and O. Takai, "Estimation of the Electricity Storage Volume Density of Compact SMESs of a New Concept Based on Si Microfabrication Technologies," Magnetochemistry, vol. 7, no. 3, p. 44, Mar. 2021, doi: 10.3390/magnetochemistry7030044.

[11] J. Cao and A. Emadi, "A New Battery/UltraCapacitor Hybrid Energy Storage System for Electric, Hybrid, and Plug-In Hybrid Electric Vehicles," in IEEE Transactions on Power Electronics, vol. 27, no. 1, pp. 122-132, Jan. 2012, doi: 10.1109/TPEL.2011.2151206.

[12] J. Li, M. Zhang, Q. Yang, Z. Zhang and W. Yuan, "SMES/Battery Hybrid Energy Storage System for Electric Buses," in IEEE Transactions on Applied Superconductivity, vol. 26, no. 4, pp. 1-5, June 2016, Art no. 5700305, doi: 10.1109/TASC.2016.2527730.

[13] Z. Song, J. Li, J. Hou, H. Hofmann, M. Ouyang, J. Du, "The battery-supercapacitor hybrid energy storage system in electric vehicle applications: A case study," Energy, vol. 154, pp. 433-441, 2018, doi: 10.1016/j.energy.2018.04.148.

[14] L. Kouchachvili, W. Yaïci, E. Entchev, "Hybrid battery/supercapacitor energy storage system for the electric vehicles," Journal of Power Sources, vol. 374, pp. 237-248, 2018, doi: 10.1016/j.jpowsour.2017.11.040.

[15] M.A. Hannan, M.M. Hoque, A. Mohamed, A. Ayob, "Review of energy storage systems for electric vehicle applications: Issues and challenges," Renewable and Sustainable Energy Reviews, vol. 69, pp. 771-789, 2017, doi: 10.1016/j.rser.2016.11.171.

[16] Y. Wang, L. Wang, M. Chen, "A review of key issues for control and management in battery and ultra-capacitor hybrid energy storage systems," eTransportation, vol. 4, 100064, 2020, doi: 10.1016/j.etran.2020.100064.

[17] Z. Jin, G. Sulligoi, R. Cuzner, L. Meng, J. C. Vasquez and J. M. Guerrero, "Next-Generation Shipboard DC Power System: Introduction Smart Grid and dc Microgrid Technologies into Maritime Electrical Netowrks," in IEEE Electrification Magazine, vol. 4, no. 2, pp. 45-57, Jun. 2016, doi: 10.1109/MELE.2016.2544203.

[18] D. Kumar and F. Zare, "A Comprehensive Review of Maritime Microgrids: System Architectures, Energy Efficiency, Power Quality, and Regulations," in IEEE Access, vol. 7, pp. 67249-67277, 2019, doi: 10.1109/ACCESS.2019.2917082.

[19] L. Hong, Q. Xu, Z. He, F. Ma, A. Luo and J. M. Guerrero, "Fault-Tolerant Oriented Hierarchical Control and Configuration of Modular Multilevel Converter for Shipboard MVdc System," in IEEE Transactions on Industrial Informatics, vol. 15, no. 8, pp. 4525-4535, Aug. 2019, doi: 10.1109/TII.2018.2879981.

[20] G. Sulligoi, D. Bosich, A. Vicenzutti and Y. Khersonsky, "Design of Zonal Electrical Distribution Systems for Ships and Oil Platforms: Control Systems and Protections," in IEEE Transactions on Industry Applications, vol. 56, no. 5, pp. 5656-5669, Sept.-Oct. 2020, doi: 10.1109/TIA.2020.2999035.

[21] L. Xu and D. Chen, "Control and Operation of a DC Microgrid With Variable Generation and Energy Storage," in IEEE Transactions on Power Delivery, vol. 26, no. 4, pp. 2513-2522, Oct. 2011, doi: 10.1109/TPWRD.2011.2158456.

[22] R. Trivedi, S. Khadem, "Implementation of artificial intelligence techniques in microgrid control environment: Current progress and future scopes", Energy and AI, vol. 8, 100147, 2022.

[23] G. Henri and N. Lu, "A Supervised Machine Learning Approach to Control Energy Storage Devices," in IEEE Transactions on Smart Grid, vol. 10, no. 6, pp. 5910-5919, Nov. 2019, doi: 10.1109/TSG.2019.2892586.

[24] S. Zhou, Z. Chen, D. Huang and T. Lin, "Model Prediction and Rule Based Energy Management Strategy for a Plug-in Hybrid Electric Vehicle With Hybrid Energy Storage System," in IEEE Transactions on Power Electronics, vol. 36, no. 5, pp. 5926-5940, May 2021, doi: 10.1109/TPEL.2020.3028154.

[25] L. Xu and D. Chen, "Control and Operation of a DC Microgrid With Variable Generation and Energy Storage," in IEEE Transactions on Power Delivery, vol. 26, no. 4, pp. 2513-2522, Oct. 2011, doi: 10.1109/TPWRD.2011.2158456.

[26] M. -E. Choi, S. -W. Kim and S. -W. Seo, "Energy Management Optimization in a Battery/Supercapacitor Hybrid Energy Storage System," in IEEE Transactions on Smart Grid, vol. 3, no. 1, pp. 463-472, March 2012, doi: 10.1109/TSG.2011.2164816.

[27] Y. Lin, L. Fu, "A novel virtual admittance droop based inertial coordination control for medium-voltage direct current ship with hybrid energy storage", Journal of Energy Storage, vol. 56, 105962, Part B, 2022, doi: 10.1016/j.est.2022.105962.

[28] D. Gonsoulin, T. Vu, F. Diaz, H. Vahedi, D. Perkins and C. Edrington, "Centralized MPC for multiple energy storages in ship power systems," IECON 2017 - 43rd Annual Conference of the IEEE Industrial Electronics Society, Beijing, China, 2017, pp. 6777-6782, doi: 10.1109/IECON.2017.8217184.

[29] M. Gaber, S. H. El-banna, M. Eldabah and M. S. Hamad, "Model and Control of Naval Ship Power System by The Concept of All-Electric Ships Based on Renewable Energy," 2019 21st International Middle East Power Systems Conference (MEPCON), Cairo, Egypt, 2019, pp. 1235-1240, doi: 10.1109/MEPCON47431.2019.9007914.

[30] M. Elmorshedy, M. M. Amin, F. F. M. El-Sousy and O. A. Mohammed, "DC-Bus Voltage Control of MPPT-based Wind Generation System Using Hybrid BESS-SMES System for Pulse Loads in Ship Power Applications," 2021 IEEE Applied Power Electronics Conference and Exposition (APEC), Phoenix, AZ, USA, 2021, pp. 76-82, doi: 10.1109/APEC42165.2021.9487114.

[31] H. Alafnan et al., "Stability Improvement of DC Power Systems in an All-Electric Ship Using Hybrid SMES/Battery," in IEEE Transactions on Applied Superconductivity, vol. 28, no. 3, pp. 1-6, April 2018, Art no. 5700306, doi: 10.1109/TASC.2018.2794472.

[32] Y. Khersonsky, "New IEEE standards for ships," 2011 IEEE Electric Ship Technologies Symposium, Alexandria, VA, USA, 2011, pp. 424-429, doi: 10.1109/ESTS.2011.5770909.

[33] K. Kim, K. Park, G. Roh, K. Chun, "DC-grid system for ships: a study of benefits and technical considerations," Journal of International Maritime Safety, Environmental Affairs, and Shipping, vol. 2, No.1, pp. 1-12, 2018, doi: 10.1080/25725084.2018.1490239.

[34] A. Hughes, B. Drury, "Chapter 8 - Field oriented control of induction motors," Editor(s): Austin Hughes, Bill Drury, Electric Motors and Drives (5th Ed.), Newnes, 2019, pp 261-305, doi: 10.1016/B978-0-08-102615-1.00008-8.

[35] B. Friedland, Control System Design: An Introduction to State-Space Methods. Mineola. NY, USA: Dover publications Inc., 2005, pp. 14-56.

[36] F. Leng, C. Tan, M. Pecht, "Effect of Temperature on the Aging rate of Li Ion Battery Operating above Room Temperature", Scientific Report, vol. 5, 12967, Aug. 2015, doi: 10.1038/srep1296.